Structure of the pygmy dipole resonance in ^{124}Sn

J. Endres,[1,*] D. Savran,[2,3] P. A. Butler,[4] M. N. Harakeh,[5] S. Harissopulos,[6] R.-D. Herzberg,[4] R. Krücken,[7,8] A. Lagoyannis,[6] E. Litvinova,[2] N. Pietralla,[9] V.Yu. Ponomarev,[9] L. Popescu,[5,10] P. Ring,[7] M. Scheck,[4,9] F. Schlüter,[1] K. Sonnabend,[11] V. I. Stoica,[5] H. J. Wörtche,[5] and A. Zilges[1]

[1]*Institut für Kernphysik, Universität zu Köln, D-50937 Köln, Germany*
[2]*ExtreMe Matter Institute EMMI and Research Division, GSI Helmholtzzentrum für Schwerionenforschung GmbH, D-64291 Darmstadt, Germany*
[3]*Frankfurt Institute for Advanced Studies, D-60438 Frankfurt am Main, Germany*
[4]*Oliver Lodge Laboratory, University of Liverpool, Liverpool L69 7ZE, United Kingdom*
[5]*Kernfysisch Versneller Instituut, University of Groningen, 9747 AA Groningen, The Netherlands*
[6]*Institute of Nuclear Physics, N.C.S.R. Demokritos Athens, GR-15310 Athens, Greece*
[7]*Physik Department, TU München, D-85748 Garching, Germany*
[8]*TRIUMF, Vancouver, British Columbia V6T 2A3, Canada*
[9]*Institut für Kernphysik, TU Darmstadt, D-64289 Darmstadt, Germany*
[10]*Belgian Nuclear Research Centre SCK*CEN, B-2400 Mol, Belgium*
[11]*Institut für Angewandte Physik, Goethe-Universität Frankfurt am Main, 60438 Frankfurt am Main, Germany*
(Received 1 April 2012; published 28 June 2012)

Background: In atomic nuclei, a concentration of electric dipole strength around the particle threshold, commonly denoted as pygmy dipole resonance, may have a significant impact on nuclear structure properties and astrophysical scenarios. A clear identification of these states and the structure of this resonance is still under discussion.
Purpose: We present an experimental and theoretical study of the isospin character of the pygmy dipole resonance and investigation of a splitting of the electric dipole strength previously observed in experiments on $N = 82$ nuclei.
Method: The pygmy dipole resonance has been studied in the semi-magic $Z = 50$ nucleus ^{124}Sn by means of the $(\alpha, \alpha'\gamma)$ coincidence method at $E_\alpha = 136$ MeV using the Big-Bite Spectrometer at the Kernfysisch Versneller Instituut in Groningen, The Netherlands.
Results: A splitting of the low-energy part of the electric dipole strength was identified in ^{124}Sn by comparing the differential cross sections measured in $(\alpha, \alpha'\gamma)$ to results stemming from (γ, γ') photon-scattering experiments. While an energetically lower-lying group of states is observed in both kinds of experiments, a higher-lying group of states is only excited in the (γ, γ') reaction. In addition, theoretical calculations using the self-consistent relativistic quasiparticle time-blocking approximation and the quasiparticle-phonon model have been performed. Both calculations show a qualitative agreement with the experimental data and predict a low-lying isoscalar component that is dominated by neutron-skin oscillations as expected for the pygmy dipole resonance. Furthermore, the states at higher energies show a pronounced isovector component and a different radial dependence of the corresponding transition densities as expected for the tail of the giant dipole resonance.
Conclusions: An experimental signature of the neutron-skin oscillation of the pygmy dipole resonance has been corroborated. The combination of the presented reactions might make it possible to identify states of this resonance.

DOI: 10.1103/PhysRevC.85.064331 PACS number(s): 24.30.Cz, 21.60.Jz, 25.55.−e, 27.60.+j

I. INTRODUCTION

The isovector electric dipole ($E1$) strength in atomic nuclei is almost completely exhausted by the isovector giant dipole resonance (IVGDR), which has been investigated intensively using various experimental approaches; see, e.g., [1] and references therein. A small fraction of a few percent of the total $E1$ strength is exhausted by the so-called pygmy dipole resonance (PDR), a concentration of $J^\pi = 1^-$ states below and partly above the particle threshold [2–11]. In theoretical approaches, this resonance is often described as an oscillation of a neutron skin against a proton-neutron core [12,13]. Thus, in general, an increase of the strength with increasing number of excess neutrons forming the neutron skin is expected. Knowledge of the neutron-skin thickness is directly linked to the equation of state (EOS) of neutron-rich matter [14] and also to corresponding objects in the universe, such as neutron stars [15]. Therefore, the extension of systematic studies to additional neutron-rich nuclei including exotic nuclei is mandatory for determining the strength as a function of proton-neutron asymmetry. The first experiments using radioactive beams to study the PDR in unstable very neutron rich heavy nuclei have already been performed and show an increase of the total strength in these nuclei [5,10,16,17]. The investigation of additional neutron-rich nuclei is, furthermore,

*endres@ikp.uni-koeln.de

of particular interest because the neutron-skin thickness, $\Delta r_{n,p}$, which is given by the difference between the neutron and proton root-mean-square (rms) radii of the nucleus, can for instance be determined from the total strength of the PDR [16–18]. Furthermore, the location and strength of the PDR has an impact on the γ-ray strength function around the particle threshold [19], nucleosynthesis processes [20,21], and supernova explosion mechanisms [14]. As a consequence, an accurate determination of the total PDR strength and a microscopic understanding of its nature are highly desirable.

The most common method for studying low-lying dipole strength below the particle threshold is nuclear resonance fluorescence (NRF) [3,4,8,9,11,22–26]. Global properties of the PDR such as the location, strength, and fragmentation can be deduced. However, a structural splitting has been observed by investigations with the $(\alpha, \alpha'\gamma)$ method that gives rise to the assumption that the low-lying $E1$ strength has a distinct underlying structure [7,27]. There is a low-energy group of states with a strong isoscalar component showing a dominant surface-peaked transition density for neutrons and a high-energy group of states with a stronger isovector component. This phenomenon has been first observed in the semi-magic nucleus ^{140}Ce [7] and is confirmed in ^{138}Ba and ^{124}Sn by comparing the results obtained in NRF experiments with results from $(\alpha, \alpha'\gamma)$ coincidence measurements with $E_\alpha =$ 136 MeV [27–29]. The corresponding experiments have been performed at the Kernfysisch Versneller Instituut in Groningen (KVI), The Netherlands, using the combination of the large-acceptance Big-Bite magnetic Spectrometer (BBS) [30] and an array of large-volume HPGe detectors. Results obtained for ^{124}Sn have recently been published in a Letter together with theoretical calculations which explain the experimentally observed splitting of the low-energy $E1$ strength by a change in structure of the corresponding transition densities [27]. The question is how much of the low-lying $E1$ strength should be attributed to the PDR in order to calculate the total strength in this excitation mode. Comprehensive and detailed information about the ^{124}Sn$(\alpha, \alpha'\gamma)$ experiment and its results will be given in this paper. In Secs. II and III, the experimental setup and the data analysis will be presented, respectively. The experimental results are given in Sec. IV and will be compared to results obtained in theoretical calculations as described in Sec. V. A summary and conclusion are given in Sec. VI.

II. EXPERIMENTAL SETUP

The ^{124}Sn$(\alpha, \alpha'\gamma)$ experiment was performed at the AGOR cyclotron facility at KVI in Groningen, The Netherlands. A primary beam of $E_\alpha = 136$ MeV was guided to the scattering chamber in front of the BBS, which was used to detect the scattered α particles with high efficiency. The BBS is a two quadrupole (Q) magnets and one dipole (D) magnet (QQD)-type spectrometer with sliding quadrupole magnets to allow for different configurations. In our case, intermediate settings have been chosen, yielding a maximum solid angle of 9.2 msr. Furthermore, the BBS allows for the option to measure at forward angles including 0° with respect to the axis defined by the incident beam. The experiment was performed with the BBS set at a central angle of 3.5°, corresponding to the first maximum in the angular distribution for exciting a $J^\pi = 1^-$ state in inelastic α scattering at $E_\alpha = 136$ MeV. The solid angle of the BBS covered α-scattering angles from about 1.5° to 5.5°. The α particles are deflected and focused on the focal plane of the BBS where detection systems are mounted to determine momentum and scattering angles of the incident particle. For this purpose, the BBS is equipped with the EuroSuperNova detection system (ESN) [31,32]. The ESN consists of the focal-plane detection system (FPDS), the focal-plane polarimeter (FPP), and two scintillator planes (S1 and S2). Two vertical-drift chambers (VDCs) form the FPDS and are installed parallel to the focal plane of the BBS. The distance between the two VDCs is 23 cm, measured along the central ray to which the VDCs are tilted by 39°. Each chamber includes two planes of 240 sense wires. The X plane is orientated in the vertical direction while the U plane is tilted by 32.9° with respect to the vertical. The trace, and hence the intersection point of the particle with the focal plane, can be reconstructed by measuring the arrival time of the electrons at each wire with respect to a start timing signal derived from the scintillator planes. Therefore, the horizontal and vertical crossing coordinates of a particle with the focal plane are thus obtained for both VDCs, which are further used to determine the angles of the particle with respect to the central ray. Finally, by taking the magnetic rigidity into account, the kinetic energy of the scattered α particle can be deduced as well from the horizontal position at the focal plane.

Each plane of the scintillator detection system consists of five overlapping plastic (NE102A) paddles with thicknesses of 2 and 6 mm for S1 and S2, respectively. In our experiment the signals of S1 are used to produce the α-trigger signal with an average trigger rate of 20 kcps.

Compared to pioneering $(\alpha, \alpha'\gamma)$ measurements by Poelhekken *et al.* using NaI detectors for γ-ray detection [33], high-purity germanium (HPGe) detectors have been used for the γ-ray spectroscopy to obtain excellent energy resolution. In total, six HPGe detectors were installed in the ^{124}Sn$(\alpha, \alpha'\gamma)$ experiment to detect the subsequent γ-ray emission following the excitation of the nuclei by α particles. Each HPGe detector had a relative efficiency of about 100% (at $E_\gamma = 1.33$ MeV compared to a $3'' \times 3''$ cylindrical NaI standard detector). Two detectors are clover-type detectors (SuperClover detectors borrowed from GSI). All detectors were installed in the horizontal plane as close as possible to the scattering chamber to optimize the efficiency. In order to measure the multipolarity of the γ-ray transitions, the detectors were arranged at different angles in the reaction plane between 90° and 260° with respect to the incident beam. In total, an absolute photopeak efficiency of 0.46% at $E_\gamma = 1.33$ MeV has been achieved. The energy dependence of the efficiency has been determined with different radioactive sources (^{56}Co and ^{60}Co) with known activities and extrapolated to high energies up to 10 MeV using GEANT4 [34] Monte Carlo simulations. The geometry of the setup especially of each HPGe detector has been implemented in the simulation in great detail [35].

Hardware coincidences between the HPGe array and S1 were used to trigger the data-acquisition (DAQ) system in order to reduce its dead time. Furthermore, an aluminum plate was placed at the position of the elastically scattered α particles

TABLE I. Experimental parameters for the ^{124}Sn$(\alpha, \alpha'\gamma)$ measurement.

Target thickness	7.0(7) mg/cm^2
Isotopic enrichment	96.96%
Central BBS angle	3.5°
Beam energy	136 MeV
Collected charge	180 μC
Average beam current	0.4 pnA
Number of HPGe detectors	6
Number of HPGe crystals	12
Absolute full-energy efficiency[a]	0.46%
Average γ-trigger rate[b]	136 kHz
Average α-trigger rate[c]	20 kHz
Average coincidence rate[d]	0.79 kHz

[a]Defined by the HPGe-detector array at 1.33 MeV.
[b]Defined by the or of all HPGe detectors.
[c]Defined by S1.
[d]With a coincidence window of $\Delta t = 300$ ns.

in front of the VDCs to reduce the count rates in the ESN detectors. In order to reduce the count rates in the HPGe detectors, the beam was focused on the target instead of using the dispersion-matching mode. In the latter case, the beam could hit the target frame and produce a high background but the energy resolution of the BBS would be improved. In addition, lead shielding was installed between the HPGe array and the BBS to suppress background produced within the spectrometer. Finally, 9.5-mm-thick lead filters were placed in front of each HPGe detector to decrease the rate of low-energy photons.

A summary of the experimental parameters is given in Table I. A more detailed description of the setup can be found in Ref. [35].

III. ANALYSIS

The aim of the offline data analysis is the determination of α-scattering differential cross sections for individual dipole excitations in ^{124}Sn, i.e., the evaluation of individual transitions of the PDR instead of giving the total cross section for the whole resonance. Therefore, a number of conditions have to be applied to the raw data. In a first step, an energy calibration of the BBS and the HPGe detectors has been determined. While radioactive sources are used to calibrate the HPGe detectors, known transitions in ^{124}Sn have been used to calibrate the particle spectrometer.

In a second step, background events can be rejected by applying gates on the time spectra in the coincidence data. Figure 1 shows the time spectrum measured with one of the HPGe detectors with respect to the α-trigger signal derived from the S1 scintillator. Due to their constant time difference, real coincidences form the prompt peak that was chosen as the origin of the x axis. Random coincidences are clearly visible and form periodical peaks around the prompt peak with a time difference of 36 ns, which corresponds to the difference between subsequent beam bursts. A timing resolution of about 8 ns has been achieved; this is sufficient to separate the prompt events from background events.

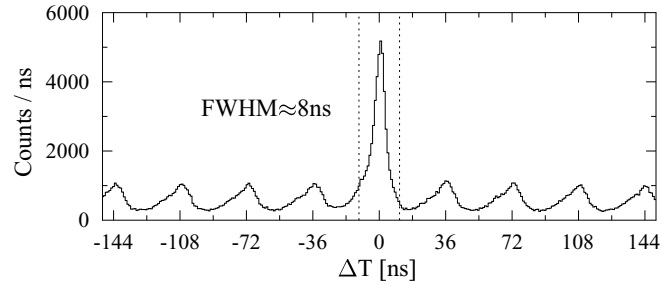

FIG. 1. Time spectrum measured with one HPGe detector with respect to the α-trigger signal derived from the S1 scintillator in coincidence mode. The prompt peak is chosen as the origin of the x axis and can clearly be separated from peaks stemming from different beam bursts. The vertical dashed lines represent the applied gate.

Further background is present at small horizontal α-scattering angles from backscattered events in the aluminum blocker of the elastically scattered α particles (see Sec. II). Hence, events with an angle smaller than $\theta = 1.6°$ are not accounted for in the analysis. All remaining events can be used to construct a coincidence matrix of the measured decay energy E_γ versus the excitation energy E_x as shown in Fig. 2.

In this matrix, γ-ray transitions occur as thin horizontal lines, which is due to the much better energy resolution of the HPGe detector array compared to the energy resolution of the particle spectrometer. The transitions into a given state of the nucleus are located on diagonal lines as indicated in Fig. 2 for the ground-state decays and for the decays into the $J^\pi = 2_1^+$ state. Hence, by applying diagonal gates on the matrix, decays into a definite final state of the nucleus can be selected and the corresponding γ-ray spectra can be generated and analyzed. Figure 3 shows these projections without any gates and with the selection of the ground-state decays. In the former case, the spectra are dominated by background

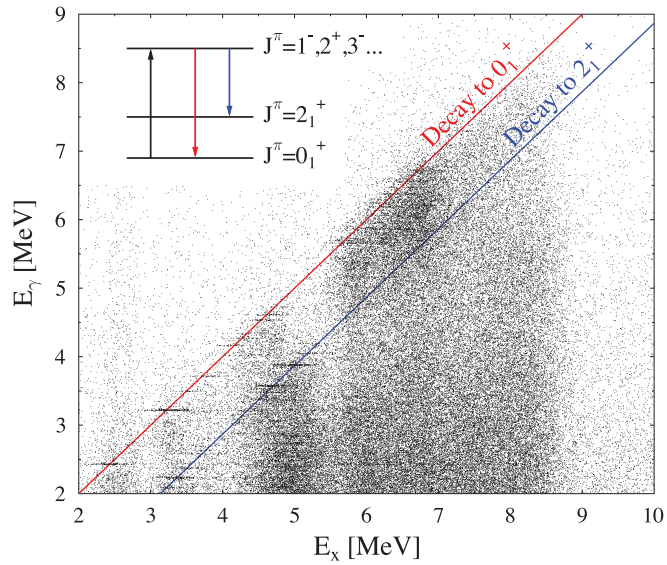

FIG. 2. (Color online) The α-γ coincidence matrix showing the γ-decay energy (E_γ) vs the excitation energy (E_x). Horizontal lines located on the diagonals indicate transitions into the ground state (red) and the first $J^\pi = 2_1^+$ state at $E_x = 1.132$ MeV (blue).

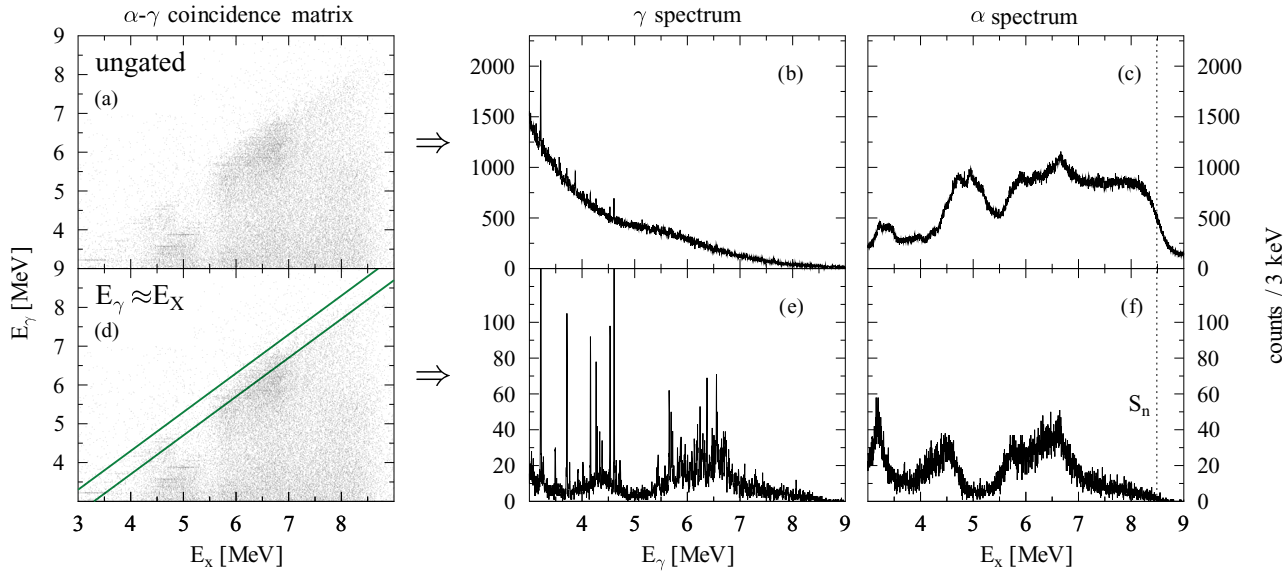

FIG. 3. (Color online) Upper row: (a) The α-γ coincidence matrix and the projections to (b) the ordinate and (c) the abscissa, without any further gates. Lower row: (a) The α-γ coincidence matrix in which the ground-state decays are selected (d, green lines), along with the corresponding (e) γ-ray and (f) α spectra. The vertical dashed lines in (c) and (f) represent the neutron separation energy, S_n, of ^{124}Sn.

and almost no individual transitions are visible. In the latter case, the spectra are almost background free and in the γ-ray spectrum strong and very well separated peaks occur, each corresponding to the decay of an excited state to the ground state. Especially the PDR between 5.5 and 7 MeV is clearly visible. It should be emphasized that, due to the high selectivity in the energy range of interest which is gained by the applied gates, no contributions of random coincidences had to be subtracted from the presented spectrum. The energy resolution for the HPGe detectors in this energy region is about 9 keV while a resolution for the BBS of about 350 keV has been achieved. The deduced ground-state decay spectra of each individual HPGe detector are the basis for the further analysis.

By analyzing the peak area, A, of each single transition, the singles differential cross sections can be deduced. The peak area in the ith HPGe detector, A_i, is related to the double-differential cross section by

$$A_i = N_t\, N_\alpha\, \Delta\Omega_\alpha\, \Delta\Omega_{\gamma,i}\, \epsilon_{\mathrm{int},i}(E_\gamma)\, \Delta_{\mathrm{live},i}\, \frac{d^2\sigma}{d\Omega_\alpha d\Omega_\gamma}, \qquad (1)$$

where N_t is the number of target nuclei per unit area, N_α is the number of incident α particles, $\Delta\Omega_\alpha$ is the solid angle of the spectrometer, $\Delta\Omega_{\gamma,i}$ is the solid angle of the HPGe detector, $\epsilon_{\mathrm{int},i}(E_\gamma)$ is the intrinsic efficiency of the germanium detector, and $\Delta_{\mathrm{live},i}$ is the relative live time of the germanium detector defined as the ratio between live and measuring time. To determine the singles α-scattering cross sections, $d\sigma/d\Omega_\alpha$, from the double-differential cross sections, the α-γ angular correlation, $W(\Omega_\gamma)$, is needed. The relation is given by

$$\frac{d\sigma}{d\Omega_\alpha} = 4\pi \frac{\Gamma}{\Gamma_0} \frac{1}{W(\Omega_\gamma)} \frac{d^2\sigma}{d\Omega_\alpha d\Omega_\gamma}, \qquad (2)$$

with the branching ratio $\frac{\Gamma_0}{\Gamma}$ to the ground state.

The uncertainties given for the cross sections in Sec. IV are statistical only. For the correct determination of the absolute values, additional systematic uncertainties have to be taken into account due to the target thickness (10%), the current integration in the Faraday cup (5%), the HPGe detector efficiencies (5%), and the calculated angular correlation (20%). However, these systematic uncertainties affect all cross sections in the same way and do not influence the relative intensities of the observed excited states.

The α-γ angular correlation shows different relative intensities depending on the angle of the HPGe detector. It is calculated using the program ANGCOR [36]. The m-state population amplitudes, needed as input for ANGCOR, result from distorted-wave Born approximation (DWBA) calculations using the program CHUCK3 [37,38]. Since optical-model parameters are needed for the input of CHUCK3, a global parametrization is taken from Ref. [39]. However, the calculated angular distributions hardly change for slightly different optical-model parameters. The values of the α-γ angular correlation depend on the scattering angles of the α particles and γ rays (θ_α, ϕ_α, θ_γ) as defined in Fig. 4.

Since the angles θ_α and θ_γ are measured with respect to the beam axis, we choose the axis for the angular correlation to be also the beam axis. While the central angle of each HPGe detector, θ_γ, is fixed, a horizontal as well as a vertical solid angle of approximately $\pm 10^\circ$ is covered. Furthermore, the BBS has a large solid angle and, therefore, an averaging of the α-γ angular correlation over the acceptance of the BBS with respect to θ_α and ϕ_α as a function of θ_γ is needed. The BBS covers α-scattering angles from about 1.5° to 5.5°. The resulting averaged angular correlation is shown in Figs. 5(a) and 5(b) for dipole and quadrupole transitions ($0 \to 1 \to 0$ and $0 \to 2 \to 0$ cascades), respectively. In addition, the distribution for the angles ($\theta_\alpha = 3.5^\circ$, $\phi_\alpha = 0^\circ$) is presented. The proportionality of the double-differential cross section,

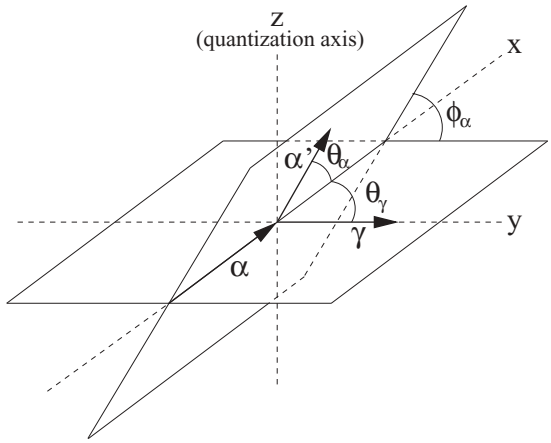

FIG. 4. Definition of angles for the α-γ angular correlation.

which can be determined for each single HPGe detector, and the angular correlation [see Eq. (2)] allow for an unambiguous assignment of the multipolarity of a certain transition. Hence, the spin of the excited state can be identified. The accuracy of the calculated α-γ angular correlation has been proven in Ref. [33].

Due to low statistics, the γ-ray spectra of the most efficient detectors for dipole transitions, which were positioned at backward angles, had to be summed in order to achieve an optimized peak-to-background ratio. The singles differential cross sections can be determined from the peak areas, A, of the sum spectrum using Eqs. (1) and (2):

$$A = N_t\, N_\alpha\, \Delta\Omega_\alpha\, \frac{\Gamma_f}{\Gamma}\, \frac{d\sigma}{d\Omega_\alpha}\, \sum_i [\Delta_{\mathrm{live},i}\, \epsilon_{abs,i}(E_\gamma)\, W_i], \qquad (3)$$

with

$$\epsilon_{abs,i}(E_\gamma) = \frac{\Delta\Omega_{\gamma,i}}{4\pi} \epsilon_{\mathrm{int},i}(E_\gamma). \qquad (4)$$

In the presented analysis, the peak area A is given by the total area F minus the background B:

$$A = F - B. \qquad (5)$$

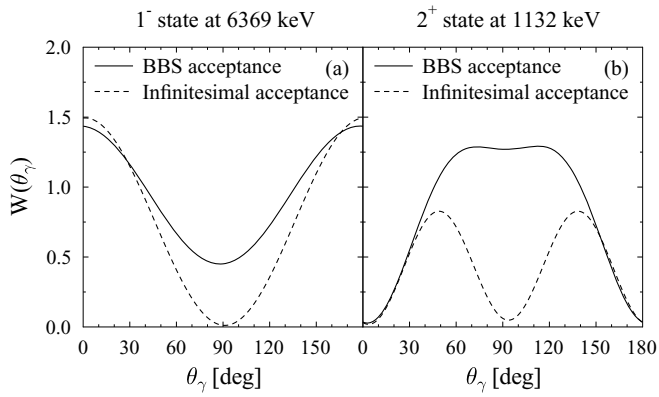

FIG. 5. Calculated α-γ angular correlations for (a) a dipole and (b) a quadrupole transition. The solid lines show the averaged angular distributions while the dashed lines represent the angular correlations for the angles ($\theta_\alpha = 3.5°$, $\phi_\alpha = 0°$).

For the statistical error of the peak area,

$$\Delta A = \sqrt{A + 2B} \qquad (6)$$

is assumed. The relative uncertainty of the peak area, $p = \frac{\Delta A}{A}$, is required to be smaller than $p \leqslant 0.3$ to be accounted for in the analysis. From this a condition for the minimum peak area follows:

$$A \geqslant \frac{1}{2p^2} + \sqrt{\frac{1}{4p^4} + \frac{2B}{p^2}}. \qquad (7)$$

Finally, A can be converted into a cross section by using Eq. (3) to present the experimental energy-dependent sensitivity limit based on the background present in the spectra.

IV. EXPERIMENTAL RESULTS

Following the procedure described in the previous section, the experimental results of the ^{124}Sn$(\alpha, \alpha'\gamma)$ experiment will be given and discussed in this section.

A. Determination of multipolarities

A ground-state decay spectrum measured with all HPGe detectors at backward angles (between 120° and 220°) in the ^{124}Sn$(\alpha, \alpha'\gamma)$ reaction is shown in Fig. 6(a). While several known $J^\pi = 2^+$ states are visible between 4 and 5 MeV, the transitions stemming from the PDR are well separated and clearly visible above 5 MeV. Figure 6(b) depicts the ground-state decay spectrum with the HPGe detectors at forward angles of around 90° and 260°. Qualitatively, the multipolarity can be identified by comparing these two spectra regarding the intensity ratio between dipole and quadrupole transitions. The former ones are very much suppressed at the forward angles of this measurement. The quantitative determination of the multipolarity, as described above, is unambiguous if enough statistics are available. An example can be seen in Fig. 7(a) for the $J^\pi = 2^+_1$ state at 1.132 MeV. Therefore, the analysis was feasible using the individual HPGe detectors.

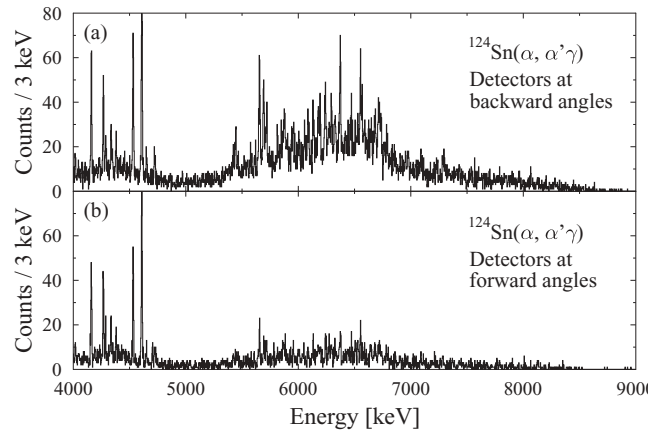

FIG. 6. Ground-state decay spectrum for the reaction ^{124}Sn$(\alpha, \alpha'\gamma)$. The summed spectra of all HPGe detectors at backward (a) and forward (b) angles are shown.

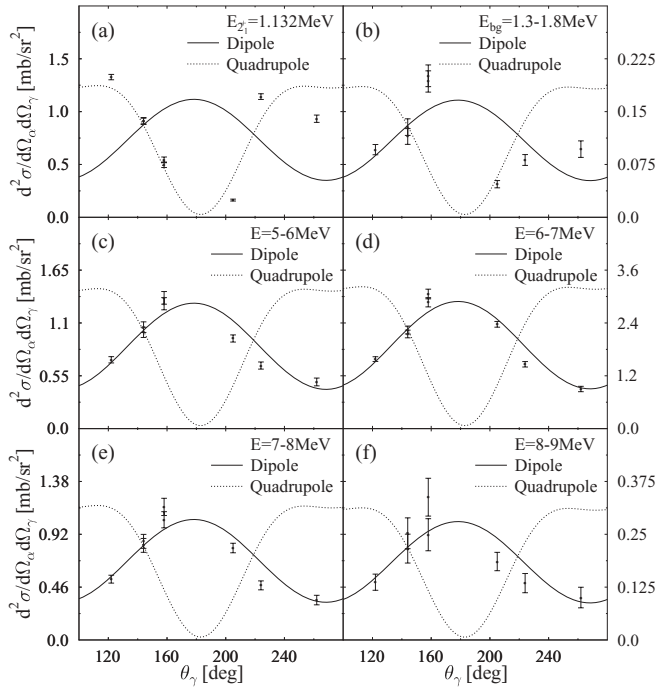

FIG. 7. Double-differential cross sections for different energy ranges in ^{124}Sn together with the averaged angular correlations for dipole (solid line) and quadrupole (dashed lines) transitions as introduced in Fig. 5. The angular correlation for the $J^\pi = 2_1^+$ state is shown in (a), a background region is shown in (b), and the PDR region between 5 and 9 MeV in a bin width of 1 MeV is shown in (c)–(f).

Unfortunately, for the energy region of the PDR, statistics are insufficient for a quantitative analysis of the angular correlation due to the small intensities at 90°. Instead, the complete spectrum in the energy region between 5 and 9 MeV in bins of 1 MeV [see Figs. 7(c)–7(f)] has been integrated for each detector. For each energy bin a multipole decomposition has been done in order to estimate the quadrupole contribution to the measured cross section. In all four cases the quadrupole fraction is consistent with zero within the uncertainties. Hence, the observed strength is of almost pure dipole character, which also demonstrates the high selectivity of the presented method to dipole transitions in the energy region of interest. Moreover, the one-to-one correlation for the present peaks in the spectra of the $(\alpha, \alpha'\gamma)$ and the (γ, γ') experiments allows for a clear identification as well. For comparison, Fig. 7(b) shows a background region which is not correlated to any certain multipolarity.

B. Determination of singles differential cross sections

As already shown, a high density of $J^\pi = 1^-$ states occur above 5 MeV. Even though the experimentally observed level spacing is of the order of the energy resolution, most peaks can be separated from each other and analyzed individually. The deduced singles differential cross sections for all identified $J^\pi = 1^-$ states measured in $(\alpha, \alpha'\gamma)$ are shown in Fig. 8(a) together with the experimental sensitivity

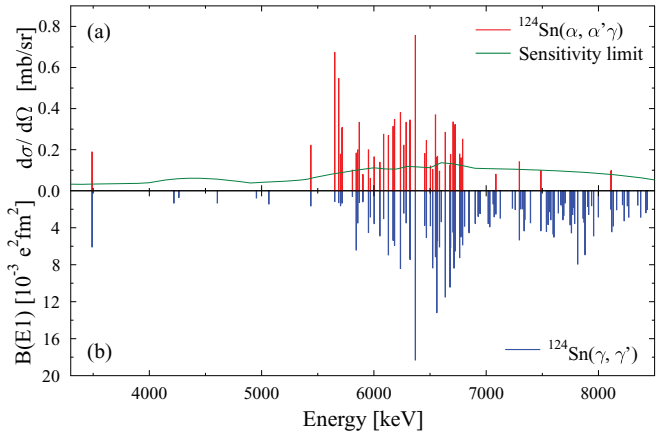

FIG. 8. (Color online) (a) Singles cross sections for the excitation of $J^\pi = 1^-$ in ^{124}Sn deduced from the $(\alpha, \alpha'\gamma)$ experiment. The solid line represents the sensitivity limit. (b) The $B(E1)\uparrow$ strength distribution, obtained in NRF [4,42].

limit. Because no significant branching into excited states was observed, $\frac{\Gamma_0}{\Gamma} = 1$ is assumed. In comparison, the results obtained in NRF measurements are given in Fig. 8(b). One (γ, γ') experiment by Govaert *et al.* [4] was conducted at the bremsstrahlung facility at the 15-MeV linac in Ghent using linearly polarized γ radiation in the entrance channel [40]. Due to the polarized beam, parities of the states have also been determined. It has to be emphasized that only natural parities are excited in the presented α-scattering experiments. Hence, negative parity is assigned to all observed $J = 1$ states in the $(\alpha, \alpha'\gamma)$ experiment. Because additional strong dipole transitions around 5.6 MeV were observed in the $(\alpha, \alpha'\gamma)$ experiment, the (γ, γ') measurement was remeasured using the Darmstadt High-Intensity Photon Setup (DHIPS) [41] at the Superconducting Darmstadt Linear Accelerator (S-DALINAC), which confirmed the additional $J = 1$ states around 5.6 MeV [42]. The corresponding values of both kinds of experiments are given in Table II.

While almost all $J^\pi = 1^-$ states have been excited and observed up to 6.8 MeV in $(\alpha, \alpha'\gamma)$ as well as in (γ, γ') reactions, the intensity drops significantly for higher energies in the case of the $(\alpha, \alpha'\gamma)$ reaction. Between 7 and 8 MeV only a few states are excited in the α-scattering experiment while a high concentration of $J^\pi = 1^-$ states with large $B(E1)\uparrow$ values has been observed in (γ, γ'). This proves that the observed splitting of the dipole strength into two parts as observed previously in the $N = 82$ nuclei ^{140}Ce and ^{138}Ba [7,29] can be confirmed in the proton magic nucleus ^{124}Sn as well. Therefore, the discussed phenomenon is independent of whether valence protons or neutrons are present.

C. Coulomb excitation

While the photons in the (γ, γ') experiments interact with the nucleus as a whole based on the electromagnetic interaction, the α particles in the present $(\alpha, \alpha'\gamma)$ experiment are predominantly isoscalar hadronic probes with an interaction located at the surface of the nucleus. Because of this different interaction depth of the two probes within the nucleus, the

TABLE II. Singles cross sections of $E1$ excitations determined from the ^{124}Sn$(\alpha, \alpha'\gamma)$ measurement and $B(E1)\uparrow$ values from the NRF experiment in Ghent [4]. All $B(E1)\uparrow$ values marked with asterisks are taken from a new measurement at the S-DALINAC at TU Darmstadt [42].

Energy (keV)	$(\alpha, \alpha'\gamma)$ $\frac{d\sigma}{d\Omega}$ (mb/sr)	(γ, γ') $B(E1)\uparrow$ ($10^{-3}\, e^2\,\mathrm{fm}^2$)
3490.18(14)	0.189(23)	6.1(7)
5438.6(4)	0.221(39)	1.64(27)*
5651.6(3)	0.673(60)	1.16(28)*
5687.0(3)	0.546(57)	1.82(30)*
5703.2(5)	0.178(45)	1.62(28)*
5716.2(10)	0.307(49)	1.34(36)*
5808.6(3)	0.101(43)	0.61(36)*
5842.5(7)	0.183(39)	6.4(5)
5856.7(20)	0.199(43)	3.48(43)*
5869.7(8)	0.333(51)	1.3(3)
5902.5(7)	0.079(43)	1.2(4)
5951.7(7)	0.199(48)	4.5(6)
5968.4(7)	0.060(32)	2.8(5)
6002.0(7)	0.165(40)	3.6(5)
6053.5(2)	0.138(57)	4.88(59)*
6086.9(4)	0.275(57)	3.01(44)*
6129.0(7)	0.269(54)	6.9(7)
6170.8(12)	0.313(54)	5.4(5)
6184.0(6)	0.347(54)	5.9(7)
6236.5(7)	0.380(63)	8.4(8)
6266.4(4)	0.221(55)	2.42(41)*
6287.1(7)	0.333(64)	3.5(6)
6321.6(7)	0.344(65)	7.4(7)
6369.1(7)	0.756(74)	18.3(11)
6453.1(7)	0.181(49)	3.7(5)
6467.5(6)	0.244(49)	5.1(5)
6503.2(6)	0.121(45)	3.8(6)
6524.0(5)	0.103(54)	8.3(9)
6548.5(5)	0.369(54)	7.1(8)
6560.8(7)	0.163(54)	13.2(12)
6565.8(8)	0.167(54)	5.4(7)
6584.1(6)	0.095(54)	6.1(6)
6635.6(6)	0.284(96)	11.5(9)
6677.9(7)	0.125(55)	10.4(9)
6683.3(8)	0.176(46)	6.1(8)
6705.4(8)	0.335(84)	4.5(6)
6713.6(7)	0.270(74)	8.4(8)
6722.3(6)	0.322(70)	6.5(7)
6764.2(8)	0.179(56)	7.2(9)
6775.6(8)	0.160(57)	5.0(9)
6790.6(8)	0.251(61)	5.8(7)
7086.5(7)	0.080(70)	2.5(4)
7295.5(7)	0.141(57)	5.3(4)
7487.6(6)	0.098(33)	4.3(6)
8111.8(16)	0.098(37)	2.0(3)

excitation of states with different radial transition densities is strongly affected. In order to prove that Coulomb excitation hardly plays a role in the excitation of the states of the PDR with the given experimental conditions in the $(\alpha, \alpha'\gamma)$ measurements, the Coulomb excitation cross sections for the given kinematic conditions and based on the $B(E1)\uparrow$ values of the single $J^\pi = 1^-$ states known from (γ, γ') have been calculated using the DWEIKO (distorted-wave eikonal approximation) code [43]. The ratio, ξ, of the thus-calculated Coulomb excitation cross sections and the measured cross sections in $(\alpha, \alpha'\gamma)$,

$$\xi = \frac{\left(\frac{d\sigma}{d\Omega}\right)_{\mathrm{Coulomb}}}{\left(\frac{d\sigma}{d\Omega}\right)_{\mathrm{experiment}}}, \tag{8}$$

is shown in Fig. 9 for each observed state. A few states show contributions larger than 20% but have also large uncertainties due to low statistics. In general, the values for ξ are calculated to be below 10%. The averaged value is 9.4%. The uncertainty-weighted average value of 2.3% is even much less. Hence, we conclude that the contribution of Coulomb excitation in our $(\alpha, \alpha'\gamma)$ experiment is negligible and the excitation of the $J^\pi = 1^-$ states is dominated by the nuclear interaction.

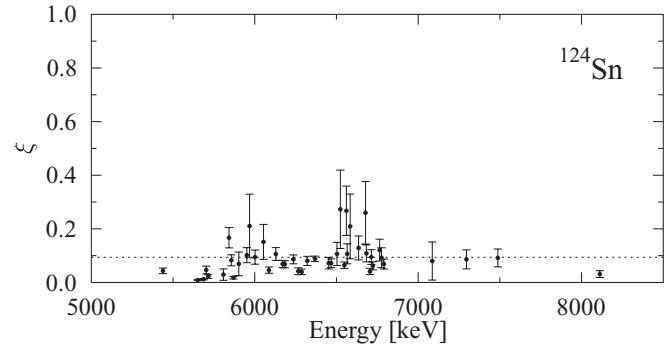

FIG. 9. Ratio ξ of the calculated Coulomb-excitation cross section and the measured cross sections in $(\alpha, \alpha'\gamma)$ for all PDR states which have been observed in $(\alpha, \alpha'\gamma)$ as well as in (γ, γ') experiments on ^{124}Sn. The horizontal dashed line represents the unweighted averaged value of 9.4%.

D. Unresolved dipole strength

Up to now, only the distinct peaks have been taken into account. However, the γ-ray spectrum shown in Fig. 6 suggests that there is additional unresolved strength above 5 MeV. The investigation of the angular distribution of the double-differential cross sections of several energy ranges up to 9 MeV, shown in Fig. 5, clearly proves the $E1$ character of this strength. In order to estimate an upper limit of its contribution, the differential cross section taking into account the complete ground-state decay spectrum has been calculated in bins of 100 keV width after subtracting the contribution of random coincidences of about 3% by gating on background peaks in the timing spectra (see Fig. 1). These integrated cross sections are depicted in Fig. 10 in comparison with the energy-integrated cross section measured with the (γ, γ') reaction. The latter represents a lower limit as discussed in Ref. [9] because here the unresolved strength was not taken into account. Erroneously, in the similar Fig. 3 in Ref. [27], the $(\alpha, \alpha'\gamma)$ and the (γ, γ') data are shifted by -50 keV and $+50$ keV, respectively.

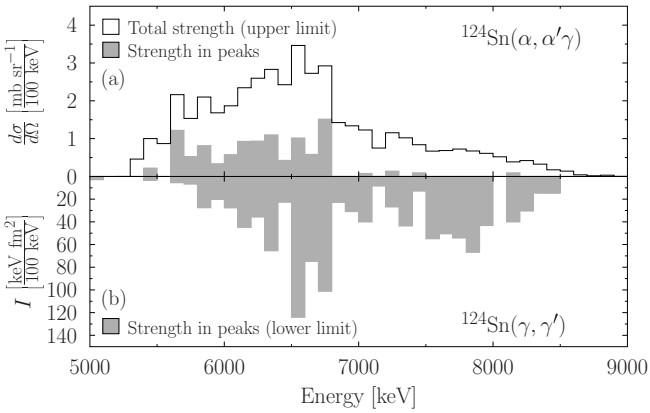

FIG. 10. (a) Differential cross sections measured in the $(\alpha, \alpha'\gamma)$ experiment integrated to bins with a width of 100 keV. The contribution of the strength resolved in single peaks is given in gray. (b) Energy-integrated cross section obtained in the (γ, γ') experiments integrated to bins with a width of 100 keV.

By taking into account the distributed dipole strength in the $(\alpha, \alpha'\gamma)$ experiment, the general picture does not change. The abrupt change of response is still clearly visible around 6.8 MeV. The cross section in $(\alpha, \alpha'\gamma)$ above 7 MeV is still significantly reduced even though the decrease of strength at higher energies is not as dramatic as when only taking single peaks into account. The ratio of the integrated cross sections in $(\alpha, \alpha'\gamma)$ in the two energy ranges, below and above 6.8 MeV, respectively, is 2.35 ± 0.03, while in the case of (γ, γ') only a factor of 1.09 ± 0.03 is observed. This clearly shows that the cross sections measured in (γ, γ') are almost equal in both energy ranges, which is not the case for $(\alpha, \alpha'\gamma)$. Furthermore, this picture would be even more distinct if the unresolved strength could be taken into account for the (γ, γ') measurement. It has to be emphasized that for both reactions $\Gamma_0/\Gamma = 1$ has been assumed to calculate cross sections and $B(E1)\uparrow$ values, respectively. Hence, the observed difference is independent of this assumption.

V. THEORETICAL CALCULATIONS

Several, partly contradictory, microscopic theoretical models exist to describe the PDR as discussed in a review by Paar *et al.* [44]. The best-applicable approaches are the quasiparticle-phonon model (QPM) [45] and (relativistic) quasiparticle random-phase approximations [(R)QRPA] [46–49]. Recently, an extension of the RQRPA model has been developed [50,51]. This relativistic quasiparticle time-blocking approximation (RQTBA) and QPM calculations have been performed in order to find a theoretical explanation of the experimentally observed splitting of the low-lying dipole strength [27].

A. Quasiparticle-phonon model calculations

The QPM employs a nuclear Hamiltonian with terms corresponding to a mean field, monopole pairing, and residual multipole-multipole interaction. The mean field is described by the Woods-Saxon potential with parameters from a global parametrization [52]. Single-particle states near the Fermi surface are adjusted so that single-particle states in the neighboring odd-mass nuclei are reproduced better in the QPM calculations. The monopole pairing strength is fixed from the data on pairing energies. The isoscalar and isovector strength parameters of the residual interaction are adjusted to reproduce the properties [excitation energy and $B(E\lambda)$ value] of collective modes of even-even mass nuclei in the QPM calculations. For example, these parameters for dipole states are fixed on the IVGDR and by setting the first 1^- QRPA solution to zero energy to exclude the center-of-mass motion.

At the first stage of the QPM calculations, the QRPA equations are solved for different multipolarities. The solutions are called phonons, which represent collective to almost pure two-quasiparticle excitations. At the next step, the wave function of excited states is written as a composition of one-phonon, two-phonon, etc. configurations. Complex two- or more phonon configurations are built up from phonons of different multipolarities, which are coupled to the same angular momentum and parity as the one-phonon component of the wave function. Interaction between different phonon configurations is calculated by employing the internal fermion structure of phonons and the QPM Hamiltonian, whose parameters are completely fixed on the QRPA level. At the final stage, the QPM Hamiltonian is diagonalized on the set of these complex wave functions.

The advantage of the QPM is that by employing a quasiboson mapping, it is possible to perform calculations on a large single-particle basis and account for complex configurations at the same time. The wave functions of the excited 1^- states in the calculations include one-, two-, and three-phonon configurations. Complex configurations are built up of phonons with λ^π from $1^\pm$ to $9^\pm$; i.e., the phonon basis is almost complete up to 9 MeV. Thus, one can expect an adequate description of the dipole strength fragmentation in the PDR region as in Refs. [9,26].

B. Relativistic quasiparticle time-blocking approximation

The RQTBA [50] for nuclear response is based on covariant energy-density functional theory (CEDFT) with an effective meson-exchange interaction. CEDFT provides the working basis for further extensions beyond the mean-field approach. Such extensions are necessitated by the fact that in medium-mass and heavy nuclei single-particle and vibrational degrees of freedom are strongly coupled. Collective vibrations lead to shape oscillations of the mean nuclear potential and, therefore, modify the single-particle motion. To take this effect into account, already in Ref. [53] a general concept for the phonon-coupling part of the single-nucleon self-energy has been proposed. The nuclear response function is described by the Bethe-Salpeter equation (BSE) in the two-quasiparticle space with an energy-dependent two-quasiparticle residual interaction which is the exact variational derivative of the phonon coupling self-energy with respect to the one-body Green's function. The BSE is solved either in the basis of Dirac states, forming the self-consistent solution of the

relativistic Hartree equations for the ground state, or in the momentum-channel representation. The approach is fully consistent: the same set of coupling constants generates the Dirac-Hartree single-quasiparticle spectrum, the static part of the residual two-quasiparticle interaction, phonon spectra, and the quasiparticle-phonon coupling amplitudes. The solution of the BSE generates excitation spectra with a multitude of 2qp ⊗ phonon (two quasiparticles ⊗ phonon) states, providing a fragmentation of the giant resonances and of the soft modes obtained in the RQRPA. The special time-projection technique blocks configurations where two quasiparticles exchange more than one phonon at the same time. The nuclear response function can then explicitly be calculated on the 2qp ⊗ phonon level by summation of an infinite series of Feynman diagrams. A special subtraction technique guarantees that there is no double counting of the correlations introduced by the particle-vibration coupling and the ground-state correlations already taken into account in the nuclear density functional. The same subtraction procedure guarantees that the spurious state, originating from translational symmetry breaking, is kept at zero energy.

The two above-mentioned tools are essential for the success of the RQTBA method. The time blocking introduces a consistent and physically justified truncation scheme into the BSE that makes it possible to solve the equations explicitly. The subtraction method is an essential tool to connect density functional theory, conventionally used only on the mean field and RPA levels, with the extended Landau-Migdal theory for the Fermi liquid, where complex configurations are included through particle-vibration coupling.

Thus, within the RQTBA the excited states are built of the (2qp ⊗ phonon) configurations, so that the model space is constructed with the quasiparticles calculated within the relativistic mean field and the phonons computed within the self-consistent relativistic QRPA. The quasiparticle space is complete up to 100 MeV. Phonons with natural parities and angular momenta up to $J = 6$ with energies below 10 MeV are included in the model space.

C. Discussion

Both models have been applied to study the low-lying electric dipole transitions in the nucleus ^{124}Sn. The electromagnetic response to the external dipole rY_1 field has been calculated with effective charges $e_p^{\text{eff}} = N/A$ and $e_n^{\text{eff}} = Z/A$. The isoscalar dipole r^3Y_1 operator, which is related to the α particles in the present experiment, has been corrected in the self-consistent RQTBA calculations by the $-\frac{5}{3}\langle r^2\rangle r$ term [54] to remove the spurious center-of-mass motion. The results are presented in Fig. 11.

In general, the QPM calculation shows a good agreement with the experimental electromagnetic strength, which is strongly fragmented into two pronounced regions at about 6.3 and 7.5 MeV. Furthermore, the calculated isoscalar strength is suppressed with increasing excitation energy, which is also in qualitative agreement with the experiment. Compared to this, the RQTBA strength is shifted by about 600 keV toward higher energies in the electromagnetic case. However, the

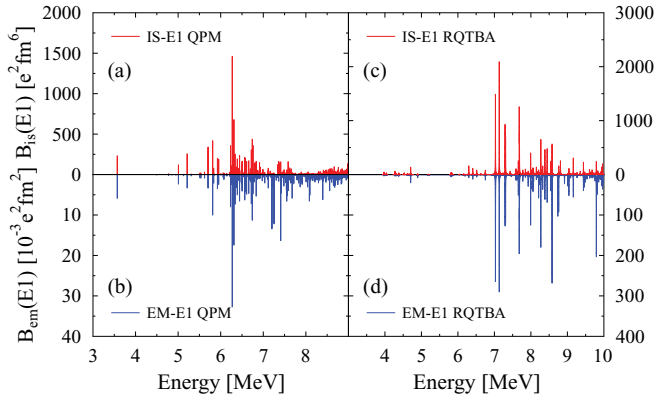

FIG. 11. (Color online) The transition probabilities in ^{124}Sn for the isoscalar (upper panels) and for the electromagnetic (lower panels) dipole operators obtained within the QPM (left) and within the RQTBA (right).

suppression of isoscalar dipole strength at higher energies is clearly visible. In order to investigate the structural difference of lower-lying and higher-lying states, the transition densities can be considered. For demonstration, two RQTBA states at 7.133 and 8.580 MeV have been studied which show similar $B_{em}(E1)$ values but differ in the $B_{is}(E1)$ case by a factor of 4. The corresponding transition densities are depicted separately for protons and neutrons in Fig. 12.

For the 7.133-MeV state, the neutron and proton contributions are in phase with a basically pure neutron contribution outside the nuclear surface, as expected for a typical state of the PDR. This can be associated with the macroscopic pictures describing the PDR as a neutron-skin oscillation against a proton-neutron core. On the other hand, a relative enhancement of the proton contribution in the nuclear medium and a reduction of the neutron component on the surface is visible for the state at 8.580 MeV. Furthermore, the neutron and proton distributions are slightly out of phase in this case. This behavior is expected for a transitional region on the tail of the IVGDR and results in a reduction of the isoscalar strength. In conclusion, this analysis shows that the energetically higher-

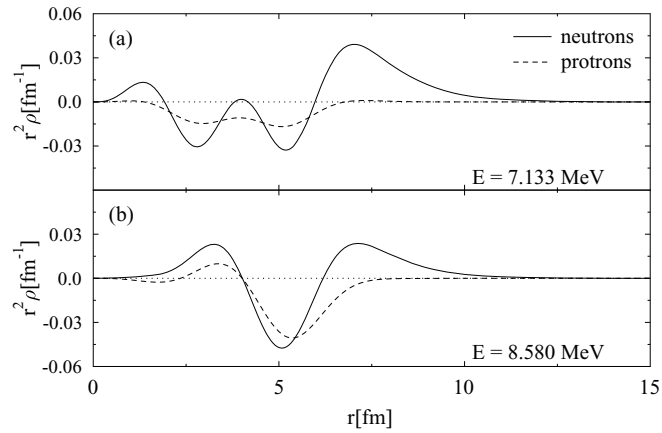

FIG. 12. Transition densities for two RQTBA states in ^{124}Sn at (a) 7.133 MeV and (b) 8.580 MeV. The contributions from neutrons and protons are shown by solid and dashed lines, respectively.

lying $J^\pi = 1^-$ states show a stronger contribution of the IVGDR and, therefore, are not or at least not strongly excited by the α particles used in the present experiment. Hence, the observed splitting can be explained by a structural difference of the discussed states while the lower-lying group of states represents the more isoscalar neutron-skin oscillation, which is interpreted as the PDR. Finally, the comparison of NRF and α-scattering experiments together with the theoretical calculations might provide a first experimental signature for distinguishing PDR states from other dipole excitations in atomic nuclei.

VI. SUMMARY AND CONCLUSION

We have investigated the $Z = 50$ nucleus ^{124}Sn with an $(\alpha, \alpha'\gamma)$-coincidence experiment using a HPGe detector array and the BBS at KVI in Groningen, The Netherlands. A high selectivity to dipole transitions by gating on ground-state transitions allowed for the identification of $J^\pi = 1^-$ states and the determination of singles differential cross sections as well as integrated differential cross sections in the energy range of the PDR. The results are compared to the $B(E1)\uparrow$ strength distribution measured in (γ, γ') by Govaert *et al.* [40] and by Schlüter *et al.* [42]. While almost all dipole transitions known from NRF experiments up to about 6.8 MeV have also been observed in $(\alpha, \alpha'\gamma)$, almost no higher-lying $J^\pi = 1^-$ states were excited by α particles under the present experimental conditions even though the strength deduced from (γ, γ') is comparably large. This observation represents further evidence for the splitting of the dipole response of atomic nuclei which has been observed up to now also in ^{140}Ce and ^{138}Ba [7,29]. The investigation of this abrupt change of dipole response is discussed for ^{124}Sn using the QPM and RQTBA models. The analysis of both calculations gives an explanation for the experimentally observed splitting. While the transition densities of the energetically lower lying group of states are dominated by a neutron oscillation on the surface of the nucleus and therefore describe typical states of the PDR, the higher-lying dipole transitions seemingly belong to a transitional region on the tail of the IVGDR, which leads to a suppression of the isoscalar response at higher excitation energies, which is in agreement with the experimental observation. In conclusion, the presented α-scattering experiments might be a first experimental signature of the neutron-skin oscillation property of the PDR in atomic nuclei and provide, in combination with NRF experiments and the interpretation based on theoretical calculations, a possibility for identifying states of the PDR.

In order to confirm this interpretation, experiments with complementary hadronic probes such as protons would be crucial. Hence, a $(p, p'\gamma)$ experiment on ^{140}Ce at KVI is planned. On the other hand, an extension of the systematics to lighter nuclei is also of great interest as would be investigating additional neutron-rich nuclei with radioactive beams.

ACKNOWLEDGMENTS

This work was supported by the Deutsche Forschungsgemeinschaft (ZI 510/4-1 and SFB 634), by the LOEWE program of the State of Hesse (Helmholtz International Center for FAIR), and by the Alliance Program of the Helmholtz Association (HA216/EMMI). The research has further been supported by the EU under EURONS Contract No. RII3-CT-2004-506065 in the 6th framework program, by the DFG cluster of excellence Origin and Structure of the Universe, by the Russian Federal Education Agency Program, and by UK STFC. The authors thank P. von Brentano, F. Iachello, H. Lenske, R. Schwengner, and A.P. Tonchev for stimulating discussions. We further thank S. Brandenburg and the accelerator staff at KVI for their support during the measurement and the GSI for lending us the SuperClover detectors.

[1] M. N. Harakeh and A. van der Woude, *Giant Resonances* (Oxford University Press, Oxford, 2001).
[2] G. A. Bartholomew, E. D. Earl, A. J. Ferguson, J. W. Knowles, and M. A. Lone, Adv. Nucl. Phys. **7**, 229 (1973).
[3] R.-D. Herzberg *et al.*, Phys. Lett. B **390**, 49 (1997).
[4] K. Govaert, F. Bauwens, J. Bryssinck, D. De Frenne, E. Jacobs, W. Mondelaers, L. Govor, and V. Yu. Ponomarev, Phys. Rev. C **57**, 2229 (1998).
[5] P. Adrich *et al.* (LAND-FRS Collaboration), Phys. Rev. Lett. **95**, 132501 (2005).
[6] S. Volz, N. Tsoneva, M. Babilon, M. Elvers, J. Hasper, R.-D. Herzberg, H. Lenske, K. Lindenberg, D. Savran, and A. Zilges, Nucl. Phys. A **779**, 1 (2006).
[7] D. Savran, M. Babilon, A. M. van den Berg, M. N. Harakeh, J. Hasper, A. Matic, H. J. Wörtche, and A. Zilges, Phys. Rev. Lett. **97**, 172502 (2006).
[8] R. Schwengner *et al.*, Phys. Rev. C **78**, 064314 (2008).
[9] D. Savran, M. Fritzsche, J. Hasper, K. Lindenberg, S. Müller, V. Yu. Ponomarev, K. Sonnabend, and A. Zilges, Phys. Rev. Lett. **100**, 232501 (2008).
[10] O. Wieland *et al.*, Phys. Rev. Lett. **102**, 092502 (2009).
[11] A. P. Tonchev, S. L. Hammond, J. H. Kelley, E. Kwan, H. Lenske, G. Rusev, W. Tornow, and N. Tsoneva, Phys. Rev. Lett. **104**, 072501 (2010).
[12] R. Mohan, M. Danos, and L. C. Biedenharn, Phys. Rev. C **3**, 1740 (1971).
[13] Y. Suzuki, K. Ikeda, and H. Sato, Prog. Theor. Phys. **83**, 180 (1990).
[14] J. Piekarewicz, Phys. Rev. C **73**, 044325 (2006).
[15] C. J. Horowitz and J. Piekarewicz, Phys. Rev. Lett. **86**, 5647 (2001).
[16] A. Klimkiewicz *et al.*, Nucl. Phys. A **788**, 145 (2007).
[17] A. Carbone, G. Colò, A. Bracco, L.-G. Cao, P. F. Bortignon, F. Camera, and O. Wieland, Phys. Rev. C **81**, 041301 (2010).
[18] O. Wieland and A. Bracco, Prog. Part. Nucl. Phys. **66**, 374 (2011).
[19] H. K. Toft *et al.*, Phys. Rev. C **81**, 064311 (2010).
[20] S. Goriely, Phys. Lett. B **436**, 10 (1998).
[21] E. Litvinova, H. Loens, K. Langanke, G. Martínez-Pinedo, T. Rauscher, P. Ring, F.-K. Thielemann, and V. Tselyaev, Nucl. Phys. A **823**, 26 (2009).

[22] T. Hartmann, J. Enders, P. Mohr, K. Vogt, S. Volz, and A. Zilges, Phys. Rev. C **65**, 034301 (2002).
[23] U. Kneissl, N. Pietralla, and A. Zilges, J. Phys. G **32**, R217 (2006).
[24] R. Schwengner, A. Wagner, Y. Fujita, G. Rusev, M. Erhard, D. De Frenne, E. Grosse, A. R. Junghans, K. Kosev, and K. D. Schilling, Phys. Rev. C **79**, 037303 (2009).
[25] N. Benouaret *et al.*, Phys. Rev. C **79**, 014303 (2009).
[26] D. Savran *et al.*, Phys. Rev. C **84**, 024326 (2011).
[27] J. Endres *et al.*, Phys. Rev. Lett. **105**, 212503 (2010).
[28] J. Endres *et al.*, AIP Conf. Proc. **1090**, 357 (2009).
[29] J. Endres, D. Savran, A. M. van den Berg, P. Dendooven, M. Fritzsche, M. N. Harakeh, J. Hasper, H. J. Wörtche, and A. Zilges, Phys. Rev. C **80**, 034302 (2009).
[30] A. M. van den Berg, Nucl. Instrum. Methods B **99**, 637 (1995).
[31] B. A. M. Krüsemann *et al.*, Nucl. Instrum. Methods Phys. Res. A **431**, 236 (1999).
[32] H. J. Wörtche for the EUROSUPERNOVA Collaboration, Nucl. Phys. A **687**, 321c (2001).
[33] T. D. Poelhekken, S. K. B. Hesmondhalgh, H. J. Hofmann, A. van der Woude, and M. N. Harakeh, Phys. Lett. B **278**, 423 (1992).
[34] S. Agostinelli *et al.*, Nucl. Instrum. Methods Phys. Res. A **506**, 250 (2003).
[35] D. Savran, A. M. van den Berg, M. N. Harakeh, K. Ramspeck, H. J. Wörtche, and A. Zilges, Nucl. Instrum. Methods Phys. Res. A **564**, 267 (2006).
[36] M. N. Harakeh and L. W. Put, program ANGCOR, KVI internal report 67i, 1979 (unpublished).
[37] P. D. Kunz, program CHUCK, University of Colorado (unpublished).
[38] J. R. Comfort and M. N. Harakeh, program CHUCK3, modified version of CHUCK, 1979 (unpublished).
[39] M. Nolte, H. Machner, and J. Bojowald, Phys. Rev. C **36**, 1312 (1987).
[40] K. Govaert *et al.*, Nucl. Instrum. Methods Phys. Res. A **337**, 265 (1994).
[41] K. Sonnabend *et al.*, Nucl. Instrum. Methods Phys. Res. A **640**, 6 (2011).
[42] F. Schlüter (private communication).
[43] C. A. Bertulani, C. M. Campbell, and T. Glasmacher, Comput. Phys. Comm. **152**, 317 (2003).
[44] N. Paar, D. Vretenar, E. Khan, and G. Colò, Rep. Prog. Phys. **70**, 691 (2007).
[45] V. G. Soloviev, *Theory of Atomic Nuclei: Quasiparticles and Phonons* (Institute of Physics, Bristol, 1992).
[46] D. Vretenar, N. Paar, P. Ring, and T. Nikšić, Phys. Rev. C **65**, 021301 (2002).
[47] N. Paar, P. Ring, T. Nikšić, and D. Vretenar, Phys. Rev. C **67**, 034312 (2003).
[48] N. Paar, T. Nikšić, D. Vretenar, and P. Ring, Phys. Lett. B **606**, 288 (2005).
[49] N. Paar, Y. F. Niu, D. Vretenar, and J. Meng, Phys. Rev. Lett. **103**, 032502 (2009).
[50] E. Litvinova, P. Ring, and V. Tselyaev, Phys. Rev. C **78**, 014312 (2008).
[51] E. Litvinova, P. Ring, V. Tselyaev, and K. Langanke, Phys. Rev. C **79**, 054312 (2009).
[52] V. Yu. Ponomarev, V. G. Soloviev, C. Stoyanov, and A. I. Vdovin, Nucl. Phys. A **323**, 446 (1979).
[53] A. Bohr and B. R. Mottelson, *Nuclear Structure*, Vol. II (Benjamin, New York, 1975).
[54] N. Giai and H. Sagawa, Nucl. Phys. A **371**, 1 (1981).